ACS SENSORS

pubs.acs.org/acssensors

Article

Sensitive Spatially Multiplexed Profiling of miRNA in Plant Tissue Using Multispectral Rolling Circle Amplification in Nanoliter Well Arrays

Jennifer Fang, Omar N. Mohd, and Patrick S. Doyle*

Cite This: https://doi.org/10.1021/acssensors.6c01105

Read Online

ACCESS | Metrics & More | Article Recommendations | Supporting Information

ABSTRACT: Quantifying the spatial distribution of microRNAs (miRNAs) within plant tissue is critical for deciphering cell-specific gene-regulatory pathways. While numerous miRNAs are involved in plant response pathways, traditional spatial miRNA detection techniques are limited to simultaneously profiling two miRNAs with a limited dynamic range. We introduce an advanced spatial profiling approach using multispectral imaging in which miRNAs are uniquely identified with spectrally distinct, minimally overlapping fluorophores. Spectral multiplexing is performed using functionalized DNA probes fixed within hydrogel posts located in nanoliter well arrays that contain both miRNA-specific and fluorophore-specific regions, enabling concurrent labeling using five fluorophores. We integrate spectral multiplexing with rolling circle amplification (RCA) to improve sensitivity and dynamic range by amplifying binding events using a DNA concatemer specific to each fluorophore. We achieved multiplex miRNA detection using five unique fluorophores, with a fluorophore-specific detection limit ranging from 1.9 to 19 zeptomoles, all within a single gel post. We showed that multispectral RCA enhances detection and quantifies low-abundance targets in ethanol-fixed, paraffin-embedded *Arabidopsis thaliana* leaf sections. Integrating multispectral RCA with our nanoliter well array enhances multiplexing by 5-fold per post and expands the utility of the technique for miRNA spatial profiling in plant tissue.

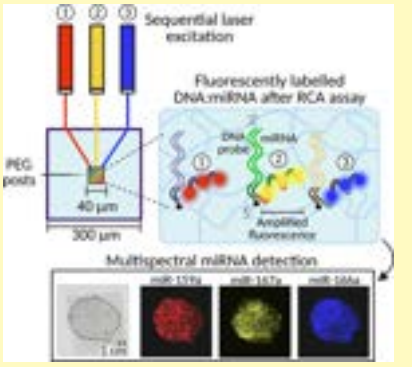

KEYWORDS: *plant microRNA, multiplexed detection, multispectral fluorescence imaging, spatially resolved quantification, signal amplification, rolling circle amplification (RCA)*

The spatial distribution of biomolecules within plants is a principal interest in understanding plant development and function, as it elucidates physiological and pathological responses before visible phenotypic changes arise. microRNAs (miRNAs) are short (20–24 nucleotide) noncoding RNAs implicated as crucial post-transcriptional regulators in plant development.[1] Since plant miRNAs bind to messenger RNA (mRNA) targets with near-perfect complementarity to regulate gene expression, cellular homeostasis is maintained through miRNA specificity, resulting in a stable and precise indicator for plant health.[2] Spatially resolved miRNA detection uncovers an additional dimension of information lost in bulk assays. Evaluating coordinated spatial gradients provides fundamental insights into how localized cell-specific gene regulation affects plant growth and development.[3] Despite the characterization of hundreds of miRNAs in plant species such as model *Arabidopsis thaliana*,[4] traditional spatial profiling methods are limited to detecting only seven plant miRNAs simultaneously across separate sections.[5] Given numerous regulatory plant miRNAs, higher-order multiplexing capabilities are needed to achieve sufficient spatial profiling.

Standard multiplexing approaches for plant miRNA have employed northern blot, multiplexed RT-PCR, electrochemical detection, and fluorescence readout techniques.[6−8] Fluorescence detection has been popularized in clinical settings due to its high sensitivity, specificity, and the variety of fluorophores used both on-sensor and in solution (non-spatial). Groups have used solution-based, fluorophore-specific single-target detection with RT-qPCR[9] and FRET[10,11] at a 3-plex limit and with electrochemical methods[12] at a 5-plex limit. Spatial-based methods use fluorescence in situ hybridization (FISH), relying on simultaneous 2-plex miRNA detection within cells.[13] A significant limitation of fluorescence-based detection is spectral overlap, which maintains clear signal differentiation up to six colors due to fluorophore properties and scanner bandpass filters. While spectral unmixing uses combinatorics to surpass the 6-plex limit,[14] significant assay complexity and advanced deconvolution algorithms are required, making fluorophore-specific single-target detection a more straightforward approach.

Received: March 13, 2026
Revised: June 5, 2026
Accepted: July 14, 2026

ACS Publications

© XXXX American Chemical Society

Downloaded from http://pubs.acs.org/ascef/article-pdf/doi/10.1021/acssensors.6c01105/6390848/se-2026-01105h.pdf by MASSACHUSETTS INST OF TECHNOLOGY user on 10 August 2026

Beyond multiplexing, low expression levels and post-processing challenges (secondary metabolites[15] and miRNA methylation[16]) make detection difficult. There is a need to combine spectral multiplexing with an amplification workflow to detect low transcript levels. While contemporary methods such as spatial imaging-based MERFISH[17] and sequential FISH (seqFISH)[18] are designed for mRNA, analogous approaches for amplifying miRNA signatures using fluorophore-specific, multiplexed detection remain largely unexplored. In our group, we have used a single-fluorophore approach to spatially quantify and amplify the miRNA signal with the nanoliter well array technique.[19] This technique uses porosity-tuned hydrogels composed of permeable semi-interpenetrating PEG networks to enable rapid miRNA diffusivity into hydrogel posts followed by localized hybridization to uniformly incorporated DNA probes (via complementary target miRNA sequence).[20] Furthermore, highly permeable hydrogels enable diffusion of fluorescently conjugated proteins (SA-PE, hydrodynamic radius ~20 nm) with spatial miRNA detection across complex plant and mammalian tissue types.[19,21]

Improving signal sensitivity has been explored using isothermal rolling circle amplification (RCA). The amplification scheme, adapted from fundamental RCA techniques, consists of four parts[22,23]: linear DNA circularizes to form a circular template, circles then anneal to a primer (adaptor), and phi29 DNA polymerase elongates the adaptor to yield an extended concatemer composed of tandem repeats containing the initial complement of the template.[22] Multiple fluorophore-conjugated reporters then bind to the concatemer, where imaging appears as a bright, single-molecule spot associated with a single captured miRNA,[23] greatly improving the assay detection limit. RCA linearly amplifies the detection probes after target hybridization rather than the target itself, increasing specificity and reducing quantification biases expected in RT-qPCR.[24] Previously, we integrated RCA with the well array technique to achieve zeptomole-level sensitivity;[25] however, because prior methods used a single fluorophore (SA-PE) for detection, multiplexing capacity was limited by the number of posts that could be fabricated in each well (7-plex limit, including two control posts). Relying on a single optical channel imposes a trade-off between achieving the desired multiplexing capability and adhering to spatial constraints.

In this work, we report an advanced multispectral RCA technique that expands spatial miRNA profiling from single-plex to 5-plex within a single hydrogel post. To ensure clarity of the workflow, Figure 1 shows the multispectral RCA assay of a representative 3-plex subset. Increased multiplexing is achieved by pairing target-specific probes with spectrally distinct fluorophores and imaged using corresponding single-channel filters to minimize spectral overlap. DNA probes contain the modified miRNA complement and a fluorophore-specific adaptor for spectrally- and spatially-resolved resolution (Figure 1A).

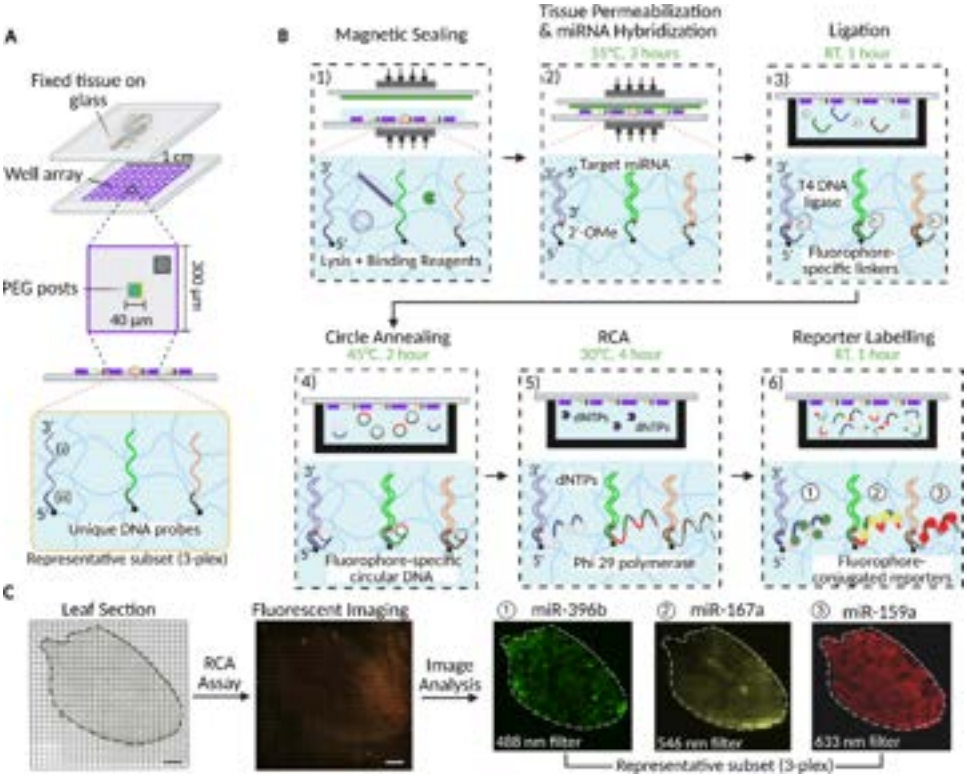

Figure 1. (A) Nanoliter well array device construction and visualization of the probe design. The 1 cm^2 array comprises of NOA 81 wells with individual feature sizes of 300 μm × 300 μm × 40 μm. Sequence-specific DNA probes are crosslinked to the PEG hydrogel backbone as 40 μm × 40 μm square posts. Each miRNA target post (depicted in the well center) contains five unique DNA probes with different sequences that are (i) complementary to a single miRNA sequence and (ii) detectable by a unique fluorophore, enabling detection of five unique targets in one post (three are represented). After hydrogel posts are fabricated, plant tissue is sandwiched over the array. (B) Schematic of the (1) miRNA hybridization and (2) ligation, followed by the (3–6) spectrally differentiated RCA assay, with sequential binding steps occurring in molecular detail demonstrating fluorophore-specific detection. (C) Advanced detection scheme using fluorophores with minimal spectral overlap to identify five unique targets by wavelength and quantify miRNA amounts in a single hydrogel post (shown as a representative 3-plex panel). Scale bars are 1 mm.

https://doi.org/10.1021/acssensors.6c01105
ACS Sens. XXXX, XXX, XXX–XXX

Downloaded from http://pubs.acs.org/ascef/article-pdf/doi/10.1021/acssensors.6c01105/6390848/se-2026-01105h.pdf by MASSACHUSETTS INST OF TECHNOLOGY user on 10 August 2026

During tissue processing, reagents liberate miRNA from plant tissue, enabling diffusion into hydrogels and DNA probe hybridization, followed by fluorophore-specific adaptor ligation to an RNA: DNA duplex (Figure 1B). To increase sensitivity with multispectral specificity, RCA pairs a fluorophore-specific circular template with a corresponding adaptor during annealing, prior to simultaneous amplification. After RCA, the concatenated DNA product binds to complementary fluorophore-specific reporters, preserving the fundamental RCA workflow within the multispectral framework (Figure 1B). Our optimized technique is applied to *Arabidopsis thaliana* leaf sections, and the spectrally resolved RCA output is visualized as a color-specific heatmap (Figure 1C, representative 3-fluorophore subset). The novelty of the multispectral RCA method lies in its 5-fold multiplexing enhancement per post and an increased sensitivity of up to 50-fold. Since multispectral RCA has not previously been applied at the 5-plex level, this platform approaches the limits of single-channel multispectral imaging, enabling greater spatial profiling of previously undetectable miRNAs critical to plant development. The multispectral RCA platform expands the landscape of spatial transcriptomics, offering a versatile tool for profiling miRNAs across diverse tissue types.

■ EXPERIMENTAL SECTION

Arabidopsis Growth, Processing, and Sectioning

Arabidopsis (Col-0) seeds were dried and stored in tubes before being sown by scattering directly onto the soil. Soil mix is 3 parts germination mix (Lambert LM-2 Germination Mix), 1 part vermiculite, and Osmocote 14-14-14 (slow-release fertilizer). Following sowing, pots were stratified for 4 days at 4 °C with no light to ensure synchronous germination before being transferred for continual growth. Conditions for Arabidopsis growth, along with tissue fixation, paraffin embedding, and sectioning methods, were defined according to the previously described protocol,[21] with additional details provided in Addendum S1.

Device Fabrication

Nanoliter well arrays were fabricated according to established protocols.[19] Experimental details provided in Addendum S2. After fabricating the well arrays, the established protocol was modified during hydrogel post fabrication within each well by combining DNA probes (Integrated DNA Technologies) with an adjusted precursor base to form the prepolymer solution. Resuspended DNA probes (1 mM stock in 1 × Tris-EDTA (1 × TE) buffer, Table S1) were added to a precursor base comprised poly(ethylene glycol) (PEG, 200 g/mol), PEG diacrylate (PEGDA, 700 g/mol), and Darocur 1173 photoinitiator (2-hydroxy-2-methylpropiophenone) (PI) in 1xTE buffer. To accommodate both single-target and multiplexed miRNA assay configurations within a single post, the relative volume of the probe-containing 1 × TE fraction was adjusted while maintaining a fixed combined volume of 40 μL (Table S3). The final working prepolymer solution has a standard composition of 36% (v/v) PEG, 18% (v/v) PEGDA, 4.5% (v/v) PI, and 41.5% (v/v) ∼1 × TE buffer (including DNA probes). Prepolymer washing and subsequent photopolymerization steps for post fabrication along with potassium permanganate rinsing and storage are provided in Addendum S2 according to prior protocols.[19]

Spectral Multiplexing miRNA Assay Protocol

Reagents and tissue preparation prior to the full miRNA hybridization workflow are performed using established protocols.[19] Experimental details provided in Addendum S3. After target hybridization, we modify the established ligation protocol by combining all fluorophore-specific adaptors containing 250 μL ligation solution and introduced to the array with 1 h incubation at room temperature in the dark. The ligation solution consists of 85.3% (v/v) 1 × TET, 10% (v/v) 1 x NEBuffer 2 (New England Biolabs), 2.5% (v/v) 10 mM ATP (New England Biolabs), 0.2% (v/v) 800 μg/mL T4 DNA ligase (New England Biolabs), and 0.4% (v/v) 1 mM for each adaptor (2% v/v 1 mM total adaptor).

Circular DNA Synthesis and Validation

Circularized DNA was synthesized according to prior techniques.[25] Experimental details are described in Addendum S4.

Multispectral RCA Assay Protocol

Before the spectral RCA assay, miRNAs hybridize to fluorophore-specific DNA probes to form RNA:DNA duplexes, allowing RCA adaptor ligation (Integrated DNA Technologies) complementary to fluorophore-specific circular templates (Figure 1B). During circular annealing, fluorophore-specific circular DNA templates (each at 150 nM) are combined and incubated on the array at 45 °C for 2 h. To prevent array drying, we use prior techniques.[25] Excess circular templates were removed after annealing, and RCA buffer was introduced to the array. The buffer consists of working concentrations of 1 × NEBuffer 2 (New England Biolabs), 200 μg/mL bovine serum albumin (BSA, New England Biolabs), 280 μM (each) deoxy nucleoside triphosphates (dNTPs, New England Biolabs), 5 mM dithioerythritol (DTT, Thermo Fisher Scientific), and 400 U/mL phi29 DNA polymerase (New England Biolabs). RCA was performed by incubating the array (VorTemp 56) at 30 °C for up to 4 h, depending on amplification requirements.

After RCA completion, reporter and fluorophore labeling are combined into a single step using reporters conjugated to fluorescent dyes with a modified NHS ester attachment. The array is incubated with all reporters simultaneously, with each reporter at a working concentration of 0.4 μM (total 4 μM), for 1 h at room temperature in the dark. Each fluorescent dye is detected by combining two complementary reporter sequences, each identical to the RCA-concatenated product (i.e., the circular DNA template). After removing the reporter solution, R50 is added, and the array is left at room temperature in the dark for 30 min to allow excess reporters to diffuse out of the hydrogel posts. Arrays are placed on a cover glass (18 mm × 18 mm, #1.5, VWR) for whole-slide imaging.

Data Acquisition

Fluorescently labeled arrays were sequentially imaged with a fluorescence slide scanner (TissueFAXS SL, TissueGnostics) using Allband software configurations with separate filters. Using spectra-split narrow-band filters, discrete channels were scanned for each miRNA-specific fluorophore: ss488, ss546, ss594, ss647, and ss750. To ensure a high dynamic range that accommodates both high and low miRNA levels after RCA, exposure settings were mathematically calibrated by fitting a scaling factor to convert signals across varying exposure times for different miRNAs. High-resolution scanner outputs (.aqproj format) support multiscale imaging where all experiments in this work use a 10× objective lens with a scanner resolution of 0.67 μm per pixel.

Data Analysis and Statistical Analysis

To mitigate uneven illumination imaging artifacts, stitching and shading correction algorithms were applied directly in the TissueFAXS viewer (8.0.163). Further data processing using a pixel-by-pixel signal extraction script was based on prior work,[19,25] with details in Addendum S5 that fully describe adjusting input parameters to account for experimental variations such as multispectral 5-plex detection and higher resolution image output. After input parameter modification, the signal extraction script processes raw spatial miRNA data using a two-stage (total control) correction for eliminating general and electrostatic nonspecific binding and local background noise along with manual refinement to create the preliminary miRNA heatmap for each fluorescence channel. Following established protocols,[21] a digital tissue

Downloaded from http://pubs.acs.org/ascef/article-pdf/doi/10.1021/acssensors.6c01105/6390848/se-2026-01105h.pdf by MASSACHUSETTS INST OF TECHNOLOGY user on 10 August 2026

https://doi.org/10.1021/acssensors.6c01105
ACS Sens. XXXX, XXX, XXX−XXX

mask was applied over the preliminary heatmap to define the region of interest (ROI) for thresholding and screening wells with partially filled tissue. The complete image processing workflow to generate both preliminary and final miRNA heatmaps are in Addendum S5. To compare adjacent sections, non-zero miRNA amounts within tissue ROI were averaged, with all data presented as mean ± standard deviation with tabulated coefficient of variation. Statistical significance was evaluated with either a two-tailed, unpaired t-test or one-way ANOVA. Significant ANOVA results ($p < 0.05$) are followed by post-hoc Tukey's HSD. Specific p-values and all technical replicate counts are reported within the figure captions.

■ RESULTS AND DISCUSSION

Design Considerations for Fluorophore-Based Detection

DNA probes are modified with a miRNA- and fluorophore-specific linker region, with the latter used for either (1) single fluorophore labeling or (2) amplification before detection. To construct a linker for single fluorophore labeling, we generate five separate 10-nucleotide sequences and validate them using a percent similarity threshold (<45%) to prevent nonspecific binding. We append a poly(A) tail to the end of each linker because the 3' terminal end is functionalized with an NHS ester fluorophore with a radius of gyration up to 2 nm. Extending the fluorophore away from the hydrogel matrix has been shown to improve the signal by 5-fold.[26] Additionally, five spectrally non-overlapping fluorophores were selected according to compatible fluorescent filter configurations.[27,28] Fluorophores were initially categorized by similar absorption and emission maxima, and selected based on the strongest brightness (extinction coefficient and quantum yield) for each fluorescent filter.[27] Further selection criteria include relatively low nonspecific binding and large photostability. Therefore, a combination of ATTO and Alexa Fluor (AF) dyes was selected for fluorophore-specific multiplexing (Table S1).

To integrate multispectral detection with RCA, each component of the amplification workflow is systematically evaluated: linear DNA template design for circularization, circular DNA annealing, isothermal amplification, and fluorescent reporting. The function of linear DNA in RCA is to form a circular DNA template that is the basis for an extended tandem repeated sequence. The design of optimized template sequences for multiple custom DNA oligonucleotides has been well characterized for circular DNA synthesis and downstream RCA applications.[29,30] Rational design of the DNA template and adaptors is guided by thermodynamic parameters and the consistent binding of circular DNA (GC content and melting temperature, T_m) to the adaptor[30−32] while avoiding secondary structures.[33] Using the initial RCA circular template as a reference (50% GC),[25] four original fluorophore-specific 50-nucleotide DNA circles are constructed with GC content between 30 and 70%. To mitigate nonspecific binding under established annealing conditions, DNA circles were validated using a percent similarity threshold (<45%). Circle compatibility using all five templates was validated by ensuring that the T_m is above the annealing temperature and is within 5 °C of each circle template. Matched T_m across all circular templates ensures stable annealing to the corresponding adaptor. Complementary regions between each circle and adaptor are validated by examining T_m with OligoAnalyzer (IDT) to ensure that enough Gibbs free energy can circularize the DNA template using CircLigase II and is stable after the synthesis.

After DNA template validation, the fluorophore-specific RCA adaptor is constructed to serve as the binding site for the circular template and the initiation position for amplification. The RCA adaptor is constructed with the initial non-RCA linker sequence and a complementary circular template region for annealing, thereby priming the adaptor's terminal end. After circular annealing is fully complete, RCA is performed with phi29 added for its high processivity and strand-displacement activity when paired with dNTPs and circular templates. During strand synthesis, RCA incubation time is a tunable parameter that produces a long ssDNA concatemer complementary to the circular template.[25,30] Two reporters are designed to be complementary to distinct regions of the fluorophore-specific circular template sequence, featuring an appended poly(A) tail and a terminal fluorophore functionalized with an NHS ester for direct spectrally distinct detection (Table S1). The result of RCA is a fluorescently labeled cluster localized around the miRNA probe, visualized as a distinct speckle.

Optimizing and Validating Spectral Multiplexing for Multitarget Detection

To extend the detection capacity of the current platform, target multiplexing is incorporated into a single hydrogel post, with each miRNA identified by a distinct fluorophore. Before examining target colocalization, we characterize each miRNA used for spectral detection by evaluating its individual signal contribution. Since signal contributions, including fluorescence spillover from precise miRNA binding, are determined by the intrinsic properties of each fluorophore, individual fluorophores were independently characterized and quantified for single-fluorophore spillover into unintended channels. Fluorophores are detected using the following filters: ATTO 488 (488 nm), AF 546 (546 nm), ATTO 590 (594 nm), ATTO 633 (647 nm), and AF 750 (750 nm). The reported background-subtracted signal of a particular fluorophore detected in an unintended filter is normalized to the signal from the intended filter. As shown in Figure S3, the spillover is, on average, only 1.6% of the intended signal observed at other fluorophore emission wavelengths. Notably, while ATTO 590 exhibits 23.6% spillover in the 647 nm filter (Figure S3), 500 nM of ATTO 590 is needed to yield the same signal as 20 nM of ATTO 633 using the same scanning parameters in respective target channels (data not shown). Since ATTO 633 is considerably brighter, the substantial ATTO 590 spillover contributes negligibly to the overall ATTO 633 at the same fluorophore concentration.

The signal contribution from the multiplexed system is evaluated by fabricating unique probes in separate posts at 100 μM, according to standard protocol.[21] miR-54 was fabricated separately as a negative control post since *C. elegans* is nonendogenous in plant tissue. All miRNAs were introduced to the array at 2 amol each before ligation with fluorophore-specific linkers. Targets were detected using distinct, minimally overlapping channels (Figure 2A): miR-396b (488 nm), miR-167a (546 nm), miR-156a (594 nm), miR-159a (647 nm), and miR-166a (750 nm). Figure 2A shows the alignment channel (390 nm) to clarify post locations. To quantify spectral crosstalk for each channel using individual miRNA targets in separate posts, control-subtracted non-target post signal was normalized to the primary target post signal. The resulting crosstalk between fluorescent signals ranged from 0.17 to 4.7% of the intended target post signal (Figure 2B).

Downloaded from http://pubs.acs.org/ascef/article-pdf/doi/10.1021/acssensors.6c01105/6390848/se-2026-01105h.pdf by MASSACHUSETTS INST OF TECHNOLOGY user on 10 August 2026

https://doi.org/10.1021/acssensors.6c01105
ACS Sens. XXXX, XXX, XXX−XXX

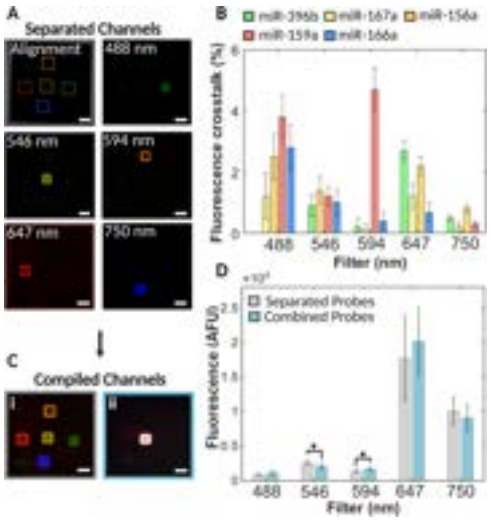

Figure 2. (A) Representative fluorescent images of five distinct DNA probes in separate hydrogel posts. Each individual channel is miRNA-specific, with the alignment focus channel (390 nm) showing all target post locations. (B) Relative crosstalk within the same channel examining off-target, nonspecific post signal using reference target signal. (C) Fluorescent images of compiled multichannel imaging with (i) five hydrogel posts in each well, each post is miRNA-specific and is detected by a unique fluorophore, and (ii) combined DNA probes with all five miRNAs captured and fluorescently labeled in one hydrogel post. Scale bar is set to 50 μm. (D) Comparative signal of each miRNA using separate and combined probes in posts within corresponding fluorescence channel. 2 amol per miRNA was added to the array with 100 μM probes each (separated posts) or 100 μM (miR-156a) and 50 μM each (for other targets) (combined post). All reported signals are total control subtracted. $*p < 0.05$, $**p < 0.01$, $***p < 0.001$ indicates statistical significance using unpaired *t*-test. Error bars represent one standard deviation with $n \geq 700$ individual posts from a single run ($N = 2$ independent replicates for validation).

To determine whether the low observed crosstalk results from minimal off-target post signal or large nonspecific contributions in the target post, all potential signal sources must be evaluated. Target post signal contributions include on-target hybridization, spectral spillover, and nonspecific miRNA binding. Non-target post signal contributions include nonspecific binding and spectral spillover. Since all miRNAs and linkers are simultaneously present, significant nonspecific miRNA binding and spectral spillover into the target channel may be misinterpreted as a low-concentration false positive in the target channel. Figure S3 reports negligible spectral spillover or relatively low fluorophore brightness in the non-target channel (ATTO 590 in 647 nm). Regarding nonspecific miRNA hybridization, prior work demonstrated minimal off-target hybridization (<3% of matched signal) for miR-167a, miR-159a, and miR-396b,[21] and targets at 1–2 base pair mismatches exhibit 3–27% off-target binding.[26] miRNA targets selected for this work share low sequence similarity (38–58%), minimizing nonspecific hybridization. While the total signal includes minor spectral spillover and nonspecific binding interactions, these additional factors are negligible relative to the true target signal, demonstrating high assay specificity in our fluorophore-specific assay.

After characterizing crosstalk in separate posts, the minimum miRNA probe concentration was optimized for the combined post to maintain a signal output similar to that of the individual probe posts (Figure S4). Decreasing the probe concentration from 100 to 50 μM did not significantly change the signal for most probes. However, a statistically significant signal reduction was observed with 50 μM miR-156a probe (Tukey's HSD, $p < 0.01$). Therefore, the miR-156a probe is set to 100 μM and the remaining four probes to 50 μM each, resulting in a combined working concentration of 300 μM per post. The combined multispectral approach was evaluated using the signal from a single post containing all five miRNA target probes along with a separate miR-54 negative control post (Figure 1A). 2 amol of each miRNA and corresponding fluorophore-specific linkers were added, and comparisons between combined and individual probes are visualized (Figure 2C), with post reproducibility illustrated using neighboring wells (Figure S5). Multiple fluorophores are incorporated into a single hydrogel post with each corresponding to a distinct miRNA-targeting probe. When comparing signal between separate and combined posts, all target channel intensities remain highly consistent, differing by less than 20% (Figure 2D).

Notably, in this multispectral approach, ATTO 488, AF 546, and AF 750 exhibited higher detection limits (0.13–0.47 amol) than the traditional multiplexing method (0.017 amol).[21] This discrepancy is due to the 5–10-fold higher brightness of SA-PE compared to the small organic fluorophores used for spectral detection. However, by consolidating all probes into a single post, the multispectral (combined-probe) approach increases multiplexing by 5-fold and reduces overall workflow time. To advance the multispectral system, we conduct further tests with multiple spectrally distinct probes integrated into a single post at a total concentration of 300 μM. RCA was used for signal amplification using a biologically relevant range of up to 2 amol of each miRNA present together.[21]

Validating and Optimizing RCA Efficacy

To detect low-abundance endogenous miRNAs, we integrated multispectral detection with RCA to enhance the sensitivity. Before RCA assay integration, linear templates were separately circularized and filtered. Circular DNA templates were validated via A260/A280 ratios (Table S4) and gel electrophoresis (Figure S6A), along with 1 h RCA to visualize characteristic speckling conducive to adaptor extension (Figure S6B).[25] Furthermore, Figure 3A shows fluorescent images of the non-RCA multispectral assay with 4 h of RCA. Increased discernible speckling within RCA posts is qualitatively observed with longer RCA times, indicating greater DNA concatemer extension. Additionally, the visual distribution of miRNA within posts remains consistent between RCA and non-RCA assays because the signal is driven by the ratio of the miRNA hybridization rate to the mass-transfer rate (Damköhler). Since target miRNAs have similar diffusion properties, the distinct signal distributions within posts reflect target-specific hybridization rates.

After RCA validation, the amplification performance of the combined probe system is compared with that of separate probe detection (standard RCA assay). The multiplexed post contains all miRNAs and circle templates, whereas the standard RCA assay added one target miRNA with the corresponding fluorophore-specific circle template. When maintaining the standard RCA protocol,[25] a significant initial 80% reduction in signal was observed (Figure S7A). We parametrically evaluated the effects of increased probe and circle concentration on the resulting signal. Introducing all DNA circles to single-target miR-167a post decreases the signal by 33% (Figure S7A). This decrease likely results from slower annealing rates driven

Downloaded from http://pubs.acs.org/ascef/article-pdf/doi/10.1021/acssensors.6c01105/6390848/se-2026-01105h.pdf by MASSACHUSETTS INST OF TECHNOLOGY user on 10 August 2026

https://doi.org/10.1021/acssensors.6c01105
ACS Sens. XXXX, XXX, XXX–XXX

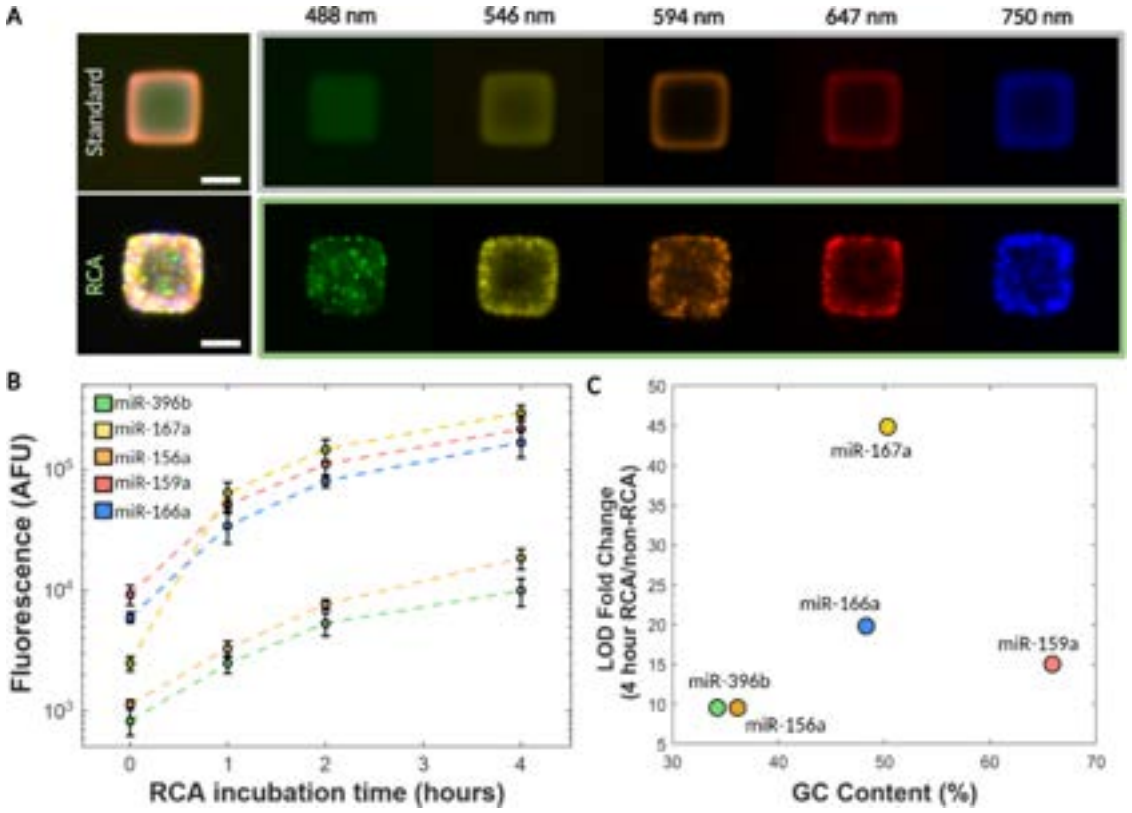

Figure 3. (A) Representative fluorescent images with combined DNA probes in a single post, and each emission wavelength targets a different miRNA (at 0.6 amol). The standard (non-RCA) protocol (top) and the RCA protocol with 4 h incubation (bottom) are shown. Characteristic speckling is also observed during RCA application. The scale bar is set to 20 μm. (B) Signal change effect over varying RCA incubation time with the total control-subtracted signal. RCA incubation time of 0 h is used as the standard (non-RCA) assay. Error bars represent one standard deviation with $n \geq 700$ individual posts from a single run ($N = 2$ independent replicates for validation). (C) Relative LOD fold change after 4 h of RCA incubation for circular templates with varying GC content. Signal from both the non-RCA and RCA assay (2 amol each) was total control subtracted before calculating the LOD. 4 h RCA assay fold change is reported relative to the standard assay. miRNA was added to the array, with probe concentrations of 100 μM (miR-156a) and 50 μM each (for other targets).

by higher total circle template concentrations, where circles form self-annealing secondary structures (primer dimers) as templates dissociate above their melting temperature (T_m).[30,34]

Probe effects were also evaluated by adding miR-167a circles across varying probe concentrations. At 300 μM total probe concentration, the signal decreased significantly by 66% (Tukey's HSD, $p < 0.01$), whereas a reduced 50 μM miR-167a probe concentration results in a negligible signal change (Figure S7B). We postulate that the signal decrease at higher total probe concentrations could result from greater DNA immobilization within the hydrogel, leading to molecular crowding and hindering mass transfer. Functionally, acrydite-modified DNA probes do not contribute to the hydrogel network, unlike PEGDA 700 crosslinking monomers. Rather, bulky polyanionic DNA ($M_W \sim 10$ kDa) creates steric hindrance and elevates negative charge density from increased probe immobilization, which could impede diffusion in the hydrogel and attenuate the readout signal.[35] To improve signal reduction caused by increased probe and circle concentration, we maintain the minimum probe concentration needed for target capture (Figure S4) and double the circle annealing time (2 h). From these modifications, the multispectral RCA protocol demonstrates near-signal recovery for most targets compared to the standard RCA approach (Figure S8).[25] Notably, while miR-156a target shows a signal enhancement after doubling the annealing time, only 50% of the signal is fully recovered.

We further optimize RCA by addressing the biochemical limits of the amplification process. Because phi29 polymerase activity is dNTP-dependent, lower dNTP levels significantly reduce DNA yield.[36] Incorporating 5-plex spectral multiplexing within each hydrogel post increases the localized amplified product by 5-fold, thus, the standard RCA workflow is reagent-limited with reduced DNA synthesis. Figure S9 shows that increasing dNTP concentrations from 150 to 280 μM nearly doubled the readout signal, indicating a dNTP-limited reaction rate (unpaired t-test, $p < 0.001$). In subsequent synthetic and tissue assay experiments, reduced probe concentration, 2 h annealing time, and 280 μM dNTPs are used. The signal change using these optimized parameters is evaluated over 4 h RCA incubation (Figure 3B), with the standard multispectral assay as the 0 h RCA incubation. All fluorophore sequences exhibited a linear increase in signal with RCA incubation time, indicating continual replication of the annealed circles and a sequence-dependent 10- and 100-fold signal amplification relative to non-RCA after 4 h.

The RCA results are used to quantify how circular template sequence construction, namely, GC content and the T_m, affects the limit of detection (LOD) for each miRNA. LOD is defined

https://doi.org/10.1021/acssensors.6c01105
ACS Sens. XXXX, XXX, XXX−XXX

Downloaded from http://pubs.acs.org/ascefj/article-pdf/doi/10.1021/acssensors.6c01105/6390848/se-2026-01105h.pdf by MASSACHUSETTS INST OF TECHNOLOGY user on 10 August 2026

as the miRNA amount related to three times the standard deviation of the 0 amol target signal. Figure 3C reports the fold change in the RCA LOD after 4 h incubation relative to the non-RCA LOD. A maximum LOD enhancement is observed at 50% GC content (a 47-fold improvement), which decreases as GC values deviate from 50% (10-fold for <40% GC content and 15-fold for >60% GC content). At lower GC content, reduced T_m decreases binding stability, potentially causing circles to dissociate from the adaptor at the annealing site. With circles above 50% GC content, increased stability can hinder RCA by circles readily forming rigid secondary structures.[34] Therefore, circular template construction should maintain GC content near 50% to achieve optimal amplification performance at a 45 °C annealing temperature.

We also note that adjusting RCA incubation time shifts the LOD, but the scanner's standard dynamic range is constrained by the accessible concentration window (after control subtraction). Therefore, while the LOD in the standard multispectral system primarily depends on intrinsic fluorophore brightness, the multispectral RCA LOD depends on fluorophore characteristics and the DNA circle sequence design, which determine annealing rates and concatemer formation. Therefore, for spectrally multiplexed systems, DNA templates and adaptors can be rationally designed and rearranged to pair with brighter fluorophores for lower-abundance miRNA detection, enhancing detection sensitivity.

Characterizing RCA Detection Performance

Optimizing the multispectral RCA process significantly improves sensitivity, but several practical considerations arise when applying miRNA detection in plant tissue. The miRNA in this work, informed by prior well array data,[21] northern blot,[37] and computational sequencing data,[38] spans both low and high expression with relevant biological amounts ranging from 0.025 to 2 amol per well. To mitigate biases due to varying GC content and fluorophore brightness, an optimized 4 h RCA incubation time was applied uniformly to ensure that the minimum expected biological miRNA amount exceeded the LOD across all miRNAs. While RCA universally enhances sensitivity, the high amplification gains required to detect low-abundance targets, along with practical scanner limitations, can cause signal saturation in abundant miRNAs. Signal saturation from RCA compromises miRNA quantification previously within the scanner's measurable range. To ameliorate this limitation, we implement a dual-scanning approach previously used to detect both high and low miRNA amounts in prior spatial miRNA-RCA work.[25] Dual-scanning uses an initial short exposure time to offset amplification-driven saturation to quantify highly expressed miRNAs. A subsequent scan uses a long exposure time (non-RCA) to fully leverage RCA sensitivity for low-abundance targets that would otherwise be below the LOD, thereby effectively increasing the workflow dynamic range. Figure 4A demonstrates that miRNA saturation at long exposures (blue boxes) was successfully resolved at shorter exposures, with saturated miRNAs rescaled for visualization.

To implement the dual-scanning approach, signal stitching between long (standard)- and short-exposure regimes using a shared miRNA amount has been applied in prior reports,[25] where characterization parameters required for signal stitching such as photobleaching susceptibility and scanner exposure settings are provided in full detail in Addendum S6. After stitching independent calibration curves and scaling at the shared miRNA amount, a single continuous curve is produced that illustrates the expanded range enabled by dual scanning (Figure 4B). After dual scanning, the rescaled calibration curves align with expected biologically relevant ranges in plant tissue. The non-RCA exposure time was established as the maximum threshold for detecting low-abundance miRNAs. While increasing exposure improves the signal-to-noise ratio (SNR) and image intensity, this limit was selected to mitigate the competing risks of elevated background noise and photobleaching. Consequently, adjusting RCA incubation time rather than

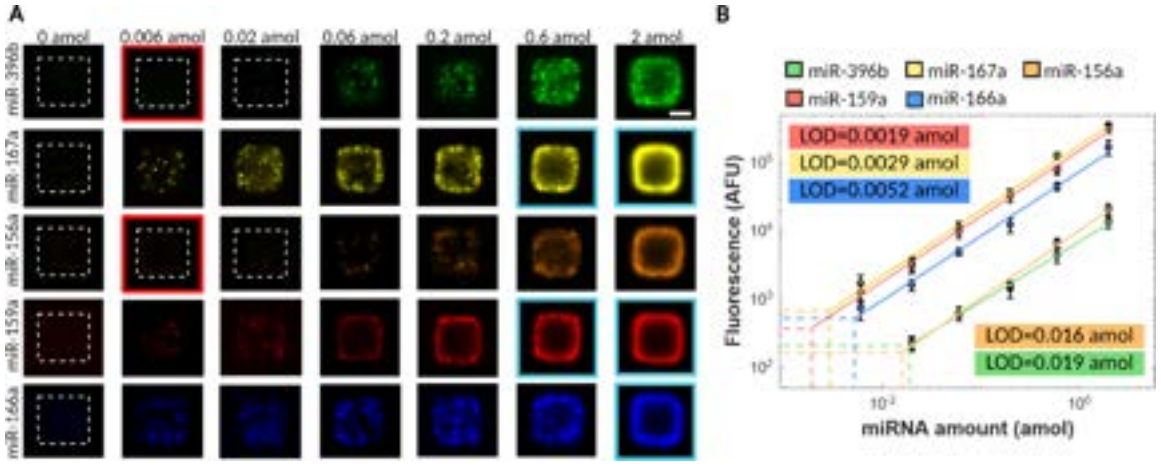

Figure 4. (A) Fluorescent representative posts of all five target miRNAs at different amounts with combined DNA probes in a single hydrogel post with a negative (miR-54) control post before performing the RCA assay. The different fluorescent channels correspond to each target. miR-396b and miR-156a were reported using the same brightness and contrast, whereas miR-167a, miR-159a, and miR-166a were reported with rescaled brightness and contrast for visualization. White dashed boxes indicate post location, red boxes indicate posts that fall below the LOD, and blue boxes indicate saturated posts at the standard (longer) exposure time. Scale bar is 20 μm. (B) Calibration curves for all five target miRNAs using RCA. miR-156a and miR-396b calibration curves were scanned at a single exposure time, and miR-167a, miR-159a, and miR-166a are rescaled calibration curves using the dual-scanning approach (Figure S12). Probe concentrations used are 100 μM (miR-156a) and 50 μM each (for other targets). Data were total control subtracted, and the dashed lines indicate the RCA LOD. Error bars represent one standard deviation with $n \geq 700$ individual posts from a single run ($N = 2$ independent replicates for validation).

https://doi.org/10.1021/acssensors.6c01105
ACS Sens. XXXX, XXX, XXX–XXX

Downloaded from http://pubs.acs.org/ascef/article-pdf/doi/10.1021/acssensors.6c01105/6390848/se-2026-01105h.pdf by MASSACHUSETTS INST OF TECHNOLOGY user on 10 August 2026

increasing exposure time is preferred to resolve miRNA below the LOD. Furthermore, miRNAs that require a dual-scanning approach for dynamic range expansion after RCA signal saturation are designed with an intrinsically bright fluorophore (ATTO 633) or an optimized adaptor/circle design (miR-167a), highlighting the need to develop a system that matches expected biological ranges.

Multiplexed Spectral RCA Detection Assay

To demonstrate well array integration with optimized spectral multiplexing, 4-week-old Col-0 *Arabidopsis thaliana* leaf tissue was profiled. Following total control subtraction (negative control (miR-54) and 0-amol subtracted) to remove any nonspecific binding effects, the standard (non-RCA) spatial profiles of three miRNAs qualitatively match the expected present tissue section location (Figure 5A). Highly abundant miR-167a is distributed across the *A. thaliana* leaf, with the absence of miRNA in the lower midrib (connecting to the petiole) characteristic of prior work.[21,39] Furthermore, we observe that initially abundant miR-166a expression also increases along the leaf perimeter, a pattern similarly characterized in spatial miR-165/166 distribution studies.[40] The miR-166a pattern is driven by high expression in abaxial cells, captured by spatial profiling that collects diverse cell types across the abaxial-adaxial axis. However, miR-156a exhibits no spatial variation, likely due to near LOD miRNA amounts, while miR-396b and miR-159a signal entirely fall below the LOD, obscuring any distinct tissue morphology (Figure 5A).

To detect lower-abundant targets and minimize sample-to-sample variability, serial sections were evaluated using the optimized 4 h RCA assay. Figure 5B shows that all target miRNAs have spatial profiles that match the locations of existing tissues, whereas only three do so in the non-RCA workflow. RCA integration specifically enabled more detailed visualization of previously undetectable profiles of miR-396b and miR-159a, while sharpening the spatial patterns of miR-167a, miR-156a, and miR-159a, as evidenced by their presence in the upper midvein (Figure 5B). miR-167a and miR-166a exhibit similar spatial profiles across the two methods, with more pronounced leaf-edge expression. When using the long exposure time for initially abundant miR-167a (Figure 5A), the signal previously below the LOD (within the lower midvein) becomes detectable after RCA, with consequent signal saturation along the leaf blade. To avoid data loss, we use the dual-scanning approach (Figure S12A) and stitch both scans into a single continuous exposure to generate a composite heatmap (Figure S13).

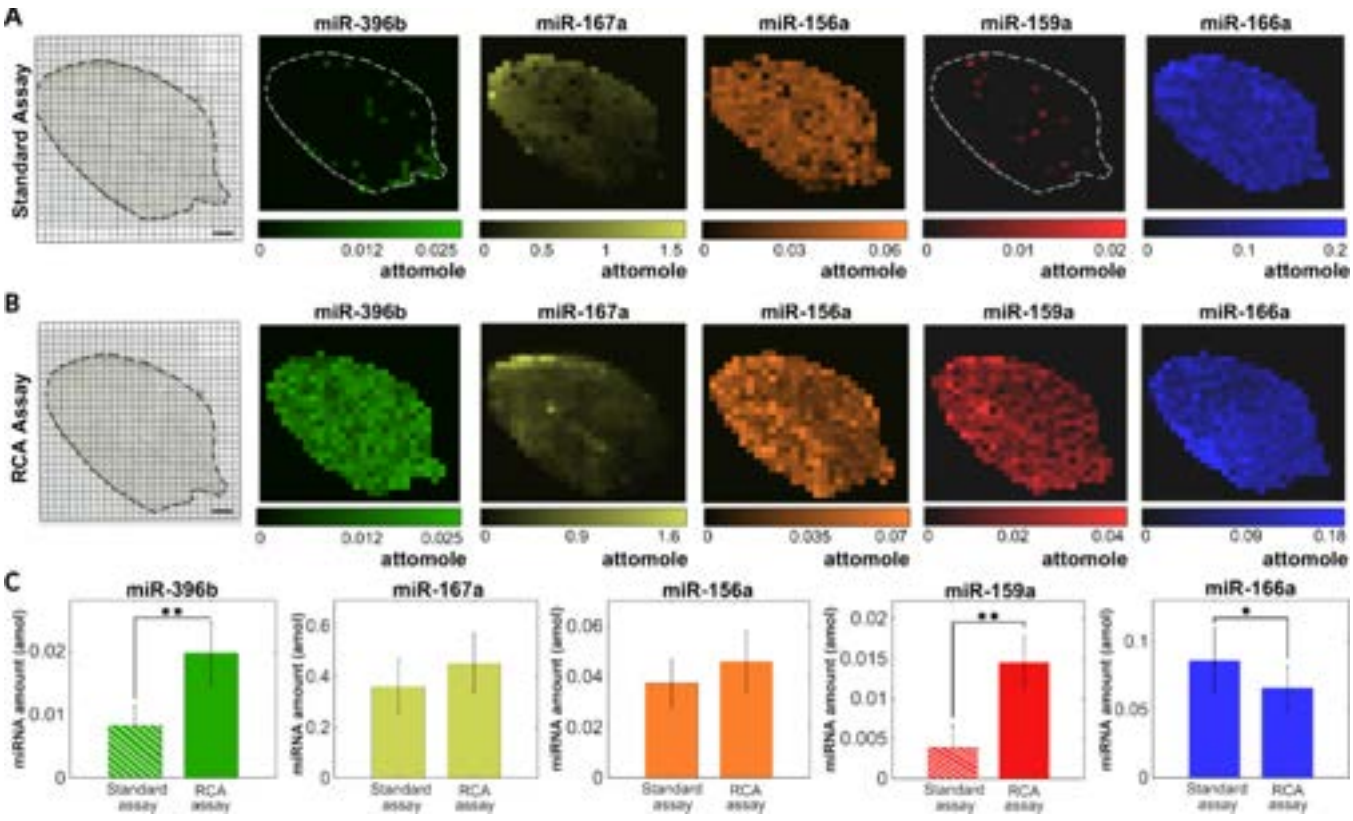

Figure 5. Comparing the performance of spectrally multiplexed miRNA detection using adjacent plant leaves in the (A) standard (non-RCA) assay and (B) RCA assay. Location of leaves in the array is outlined in black, with each well within the outline containing tissue. The 5-plex panel heatmaps are generated after miRNA extraction from leaves and a multispectral RCA assay, and are reported as miRNA amount (amol). The brightness of each pixel on the heatmap shows the amount detected in each well. In the standard assay, miRNAs below the LOD (by >10-fold) are outlined in white. In the RCA assay, miR-167a is visualized as a composite heatmap using the dual-scanning approach (Figures S12 and S13). Probe concentrations used are 100 μM (miR-156a) and 50 μM each (for other targets). The same scanner parameters are used for the standard and RCA assays. Scale bar is 1 cm. (C) Quantitative analysis of the standard assay and the RCA assay, comparing the average miRNA amount of the same target within the tissue section. Plotted data represented by hatch fill indicate averaged miRNA amounts where a majority of posts fall over an order of magnitude below the LOD. $*p < 0.05$, $**p < 0.01$, $***p < 0.001$ indicates statistical significance using unpaired *t*-test. Error bars represent one standard deviation with $n \geq 300$ individual posts from miRNAs in a single tissue section above the LOD and $n > 20$ from miRNAs below the LOD (hatch fill).

https://doi.org/10.1021/acssensors.6c01105
ACS Sens. XXXX, XXX, XXX−XXX

Downloaded from http://pubs.acs.org/ascef/article-pdf/doi/10.1021/acssensors.6c01105/6390848/se-2026-01105h.pdf by MASSACHUSETTS INST OF TECHNOLOGY user on 10 August 2026

While reducing the RCA incubation time could eliminate the need for dual scanning by bringing miR-167a amounts within the standard dynamic range, dual scanning is necessary in the 5-plex system to accommodate the wide biological range (0.01–1.7 amol) and variable LOD (0.0019–0.019 amol).

Figure 5C compares the average miRNA amounts detected by the standard and RCA assay in the tissue section. For miRNAs detectable in both workflows (miR-167a and miR-156a), the average values are quantitatively similar. For miR-166a, we observe a statistically significant decrease in the average amount after RCA (unpaired *t*-test, $p < 0.05$). This variation can result from spatial profiling along the abaxial-adaxial axis, where tissue samples may contain uneven distributions of highly expressed miR-166a in abaxial cells or an absence in adaxial cells. For low-abundance targets (miR-396b and miR-159a), the average amounts are statistically lower in the standard assay than in the RCA assay (unpaired *t*-test, $p < 0.01$), where reported miRNA signals below the LOD in the standard assay are attributed to residual analytical noise. From average values, similar trends for miR-167a, miR-159a, and miR-396b align with previous RT-PCR and traditional well array results.[21] We found that miR-167a was more abundant than miR-396b and miR-159a in both studies. Notably, the average coefficient of variation for miR-167a, miR-156a, and miR-166a across these adjacent sections is 26% (Table S5). Differences in absolute miRNA amounts between the spectral RCA and the non-spectral assay, despite consistent relative amounts, can be attributed to varying plant growth conditions, miRNA fixation preservation, and natural leaf variability.

To evaluate the reproducibility of the multispectral RCA assay, we analyzed serial sections taken from the leaf center using 4 h RCA incubation time (Figure S14). In both sections, dual-exposure scanning was used to stitch images into a composite heatmap for abundant miR-167a. The resulting spatial miRNA profiles correlate with tissue morphology between adjacent sections, demonstrating quantitative agreement, consistent relative abundances, and the high reproducibility of the multispectral RCA workflow. Across adjacent sections, similar expression patterns were maintained for each miRNA, with an average coefficient of variation of 35% (Table S5). Signal variations can be attributed to cellular heterogeneity between sections, as central leaf sections encompass varying proportions of palisade, spongy mesophyll, and epidermal cells. Overall, the relative miRNA expression in Figure S14 aligns with Figure 5B, validating robust 5-plex detection within a single hydrogel post and the recovery of lower-abundance transcripts that would otherwise be undetectable without RCA.[21]

The enhanced sensitivity from multispectral RCA helps clarify spatial biological functions from expression patterns, enabling spatial profiling of low-abundance miRNAs. Distinct spatial patterning observed for miR-167a shows decreased lower midvein expression, lending to active regulation in the vascular system.[39,41] For miR-396b, using RCA captures signal homogeneity, aligning with other studies.[42,43] miR-396b accumulation also varies across rosette leaves and increases with plant maturity, establishing its role in age signaling and phase transition regulation.[44] miR-159a exhibits higher accumulation in the leaf blade, validating prior well array studies.[21] Since miR-159a shares a distinct pattern from other members of the miR-159 family,[45] we confirm that miR-159a gradient formation modulates leaf growth and overall size.[46]

Furthermore, multispectral RCA resolves biological observations from miRNAs either undetectable or unexplored in prior well array work.[21] For instance, high miR-166a distribution along the leaf perimeter is corroborated by an LNA probe study showing that miR-166a extends radially in the abaxial domain to establish leaf polarity.[47] For miR-156a, we observe highest signal accumulation within the leaf vasculature that gradually decreased toward the leaf base, as observed with traditional histochemical staining techniques.[48] While this spatial profile is maintained across development, overall miR-156a is temporally downregulated during plant maturation, promoting the phase transition from juvenile to adult leaf.[48,49] The results confirm that multispectral RCA achieves uniform site-specific amplification, reducing target-specific biases expected in RT-PCR.[24] By consolidating all five targets into a single post and amplifying the miRNA signal with multi-channel spectral detection, multispectral RCA eliminates prior spatial-partitioning limitations from single-fluorophore studies and enhances sensitivity to spatially profile previously undetectable miRNAs in plant tissue.[21] The multispectral RCA approach provides an advanced framework for exploring crucial biological questions, such as evaluating localized, cell-specific miRNA function during plant growth and development.

■ CONCLUSION

This work integrates a multispectral detection approach with RCA to significantly enhance multiplexing capabilities from single-plex to 5-plex per post, achieving a zeptomole-level detection limit (1.9–19 zmol) for spatially resolved miRNA. Using our approach, target miRNAs are identified by specific fluorophores, enabling the colocalized detection of five distinct fluorophores within a single post. Using 4-week-old *Arabidopsis thaliana* leaf sections, two low-abundance miRNAs were otherwise undetectable without RCA. Detectable miRNAs in the standard and amplified multispectral assays showed comparable spatial profiles and consistent average miRNA expression. miRNA-dependent profiles were highly expressed along the leaf blade and in the midrib, or were homogeneously distributed, validating patterns established by traditional techniques. The multispectral RCA detection approach is a valuable addition to the ensemble of existing spatial profiling plant miRNA techniques, as prior miRNA-specific fluorophore amplification methods detect at most three targets non-spatially. Future directions using the multispectral RCA technique include increasing detection capacity up to 35 miRNAs (using seven capture posts and two controls) while preserving the original features and individual 5-plex capture post. Additionally, miRNAs can be detected in a single post, maintaining the original multiplexing capability of previous work while increasing resolution with smaller wells. Smaller wells can be applied to explore host-pathogen interactions in plants, enabling refined detection of pathogen spots as small as 500 μm.[50] The integration of multispectral RCA after target capture enables flexible miRNA profiling across multiple tissue types, establishing it as a versatile tool for spatial transcriptomics research.

■ ASSOCIATED CONTENT

Data Availability Statement

All data required to evaluate the conclusions in the paper are in the paper and the Supplementary Information. Additional data are available from the corresponding author upon reasonable request.

Downloaded from http://pubs.acs.org/ascef/article-pdf/doi/10.1021/acssensors.6c01105/6390848/se-2026-01105h.pdf by MASSACHUSETTS INST OF TECHNOLOGY user on 10 August 2026

https://doi.org/10.1021/acssensors.6c01105
ACS Sens. XXXX, XXX, XXX–XXX

Supporting Information

The Supporting Information is available free of charge at https://pubs.acs.org/doi/10.1021/acssensors.6c01105.

Experimental details for Arabidopsis growth and sectioning, device fabrication, spectral multiplexing miRNA assay protocol, circular DNA synthesis and validation, data analysis, dual-scanning approach implementation, probes and RCA-related DNA sequences with corresponding fluorophores, miRNA sequences, modified precursor composition adjusted to total probe concentrations, nanodrop results for circular DNA, coefficient of variation using adjacent samples, array and post fabrication workflow, photomask design and well array schematic, fluorophore spillover characterization, miRNA binding saturation assessment on varying probe concentrations, compiled multi-channel fluorescent images using the non-amplified multispectral approach, gel electrophoresis with circle validation, comparing RCA efficacy for probe and circle concentrations, circular annealing optimization for multispectral RCA, RCA buffer (dNTP) optimization, fluorophore photobleaching, fluorophore exposure time, calibration curves using dual-scanning approach, composite miR-167a heatmap of leaf tissue using dual-scanning approach, and multispectral RCA with adjacent sections (DOCX)

AUTHOR INFORMATION

Corresponding Author

Patrick S. Doyle – *Department of Chemical Engineering, Massachusetts Institute of Technology, Cambridge, Massachusetts 02139, USA;* orcid.org/0000-0003-2147-9172; Email: pdoyle@mit.edu

Authors

Jennifer Fang – *Department of Chemical Engineering, Massachusetts Institute of Technology, Cambridge, Massachusetts 02139, USA*

Omar N. Mohd – *Department of Chemical Engineering, Massachusetts Institute of Technology, Cambridge, Massachusetts 02139, USA;* orcid.org/0000-0002-7255-4606

Complete contact information is available at: https://pubs.acs.org/doi/10.1021/acssensors.6c01105

Author Contributions

J.F. and P.S.D. conceived the idea and designed the experiments. J.F. carried out all experiments and data analysis. O.N.M. and P.S.D. guided the research. J.F. and O.N.M. wrote the manuscript with contributions from P.S.D. All authors have given approval to the final version of the manuscript.

Notes

The authors declare no competing financial interest

ACKNOWLEDGMENTS

We thank Prof. Mary Gehring, Lindsey Bechen, and Sean Clarke (Whitehead Institute, MIT) for *Arabidopsis thaliana* plants and for supplying plant growth protocols. We also thank Dr. Jeffrey Kuhn (Koch Institute, MIT) for useful discussions on system design and data analysis. This work was supported in part by the Koch Institute Support (core) Grant P30-CA14051 from the National Cancer Institute. We thank the Koch Institute's Robert A. Swanson (1969) Biotechnology Center for technical support, specifically the microscopy, histology, and nanowell cytometry core. This material is based upon work supported by the National Science Foundation Graduate Research Fellowship under Grant No. 2141064. J.F. is an NSF Fellow at MIT. This work is in part supported by the MathWorks Engineering Fellowship. J.F. is a MathWorks Fellow at MIT. Figures were created with BioRender.com.

REFERENCES

(1) Jones-Rhoades, M. W.; Bartel, D. P.; Bartel, B. MicroRNAS and Their Regulatory Roles in Plants. *Annu. Rev. Plant Biol.* **2006**, *57*, 19–53.

(2) Yu, Y.; Wang, H.; You, C.; Chen, X. Plant microRNA Maturation and Function. *Nat. Rev. Mol. Cell Biol.* **2026**, *27* (1), 55–70.

(3) Brosnan, C. A.; Sarazin, A.; Lim, P.; Bologna, N. G.; Hirsch-Hoffmann, M.; Voinnet, O. Genome-scale, Single-cell type Resolution of microRNA Activities within a Whole Plant Organ. *EMBO J.* **2019**, *38* (13), e100754.

(4) Samelak-Czajka, A.; Wojciechowski, P.; Marszalek-Zenczak, M.; Figlerowicz, M.; Zmienko, A. Differences in the Intraspecies Copy Number Variation of Arabidopsis Thaliana Conserved and Nonconserved miRNA Genes. *Funct. Integr. Genomics* **2023**, *23* (2), 120.

(5) Válóczi, A.; Várallyay, É.; Kauppinen, S.; Burgyán, J.; Havelda, Z. Spatio-Temporal Accumulation of microRNAs Is Highly Coordinated in Developing Plant Tissues. *Plant J.* **2006**, *47* (1), 140–151.

(6) Unver, T.; Namuth-Covert, D. M.; Budak, H. Review of Current Methodological Approaches for Characterizing MicroRNAs in Plants. *Int. J. Plant Genomics* **2009**, *47*(1), 262463.

(7) Jet, T.; Gines, G.; Rondelez, Y.; Taly, V. Advances in Multiplexed Techniques for the Detection and Quantification of microRNAs. *Chem. Soc. Rev.* **2021**, *50* (6), 4141–4161.

(8) Wark, A. W.; Lee, H. J.; Corn, R. M. Multiplexed Detection Methods for Profiling MicroRNA Expression in Biological Samples. *Angew. Chem., Int. Ed.* **2008**, *47* (4), 644–652.

(9) Chinnappan, R.; Mohammed, R.; Yaqinuddin, A.; Abu-Salah, K.; Zourob, M. Highly Sensitive Multiplex Detection of microRNA by Competitive DNA Strand Displacement Fluorescence Assay. *Talanta* **2019**, *200*, 487–493.

(10) Jin, Z.; Geißler, D.; Qiu, X.; Wegner, K. D.; Hildebrandt, N. A Rapid, Amplification-Free, and Sensitive Diagnostic Assay for Single-Step Multiplexed Fluorescence Detection of MicroRNA. *Angew. Chem., Int. Ed.* **2015**, *54* (34), 10024–10029.

(11) Liu, Y.; Wei, M.; Li, Y.; Liu, A.; Wei, W.; Zhang, Y.; Liu, S. Application of Spectral Crosstalk Correction for Improving Multiplexed MicroRNA Detection Using a Single Excitation Wavelength. *Anal. Chem.* **2017**, *89* (6), 3430–3436.

(12) Hashimoto, K.; Inada, M.; Ito, K. Multiplex Real-Time Loop-Mediated Isothermal Amplification Using an Electrochemical DNA Chip Consisting of a Single Liquid-Flow Channel. *Anal. Chem.* **2019**, *91* (5), 3227–3232.

(13) Huang, K.; Baldrich, P.; Meyers, B. C.; Caplan, J. L. sRNA-FISH: Versatile Fluorescent in Situ Detection of Small RNAs in Plants. *Plant J.* **2019**, *98* (2), 359–369.

(14) Holzapfel, H. Y.; Stern, A. D.; Bouhaddou, M.; Anglin, C. M.; Putur, D.; Comer, S.; Birtwistle, M. R. Fluorescence Multiplexing with Spectral Imaging and Combinatorics. *ACS Comb. Sci.* **2018**, *20* (11), 653–659.

(15) Ghawana, S.; Paul, A.; Kumar, H.; Kumar, A.; Singh, H.; Bhardwaj, P. K.; Rani, A.; Singh, R. S.; Raizada, J.; Singh, K.; Kumar, S. An RNA Isolation System for Plant Tissues Rich in Secondary Metabolites. *BMC. Res. Notes* **2011**, *4* (1), 85.

Downloaded from http://pubs.acs.org/ascef/article-pdf/doi/10.1021/acssensors.6c01105/6390848/se-2026-01105h.pdf by MASSACHUSETTS INST OF TECHNOLOGY user on 10 August 2026

(16) Chen, F.; Fan, C.; Zhao, Y. Inhibitory Impact of 3′-Terminal 2′-O-Methylated Small Silencing RNA on Target-Primed Polymerization and Unbiased Amplified Quantification of the RNA in Arabidopsis Thaliana. *Anal. Chem.* **2015**, *87* (17), 8758–8764.
(17) Nobori, T.; Monell, A.; Lee, T. A.; Zhou, J.; Nery, J.; Ecker, J. R. Time-Resolved Single-Cell and Spatial Gene Regulatory Atlas of Plants under Pathogen Attack. *bioRxiv* **2023**.
(18) Zhu, J.; Moreno-Pérez, A.; Coaker, G. Understanding Plant Pathogen Interactions Using Spatial and Single-Cell Technologies. *Commun. Biol.* **2023**, *6* (1), 1–8.
(19) Nagarajan, M. B.; Tentori, A. M.; Zhang, W. C.; Slack, F. J.; Doyle, P. S. Spatially Resolved and Multiplexed MicroRNA Quantification from Tissue Using Nanoliter Well Arrays. *Microsyst. Nanoeng.* **2020**, *6* (1), 51.
(20) Pregibon, D. C.; Doyle, P. S. Optimization of Encoded Hydrogel Particles for Nucleic Acid Quantification. *Anal. Chem.* **2009**, *81* (12), 4873–4881.
(21) Fang, J.; Doyle, P. S. Quantitative and Spatially Resolved Detection of Multiplexed microRNA from Plant Tissue via Hybridization to Hydrogel-Bound DNA Probes in Nanoliter Well Arrays. *Microsyst. Nanoeng.* **2024**, *10* (1), 142.
(22) Garafutdinov, R. R.; Sakhabutdinova, A. R.; Gilvanov, A. R.; Chemeris, A. V. Rolling Circle Amplification as a Universal Method for the Analysis of a Wide Range of Biological Targets. *Russ. J. Bioorg. Chem.* **2021**, *47* (6), 1172–1189.
(23) Nallur, G. Signal Amplification by Rolling Circle Amplification on DNA Microarrays. *Nucleic Acids Res.* **2001**, *29* (23), e118.
(24) Ruijter, J. M.; Ramakers, C.; Hoogaars, W. M. H.; Karlen, Y.; Bakker, O.; van den Hoff, M. J. B.; Moorman, A. F. M. Amplification Efficiency: Linking Baseline and Bias in the Analysis of Quantitative PCR Data. *Nucleic Acids Res.* **2009**, *37* (6), e45.
(25) Mohd, O. N.; Heng, Y. J.; Wang, L.; Thavamani, A.; Massicott, E. S.; Wulf, G. M.; Slack, F. J.; Doyle, P. S. Sensitive Multiplexed MicroRNA Spatial Profiling and Data Classification Framework Applied to Murine Breast Tumors. *Anal. Chem.* **2024**, *96* (31), 12729–12738.
(26) Chapin, S. C.; Appleyard, D. C.; Pregibon, D. C.; Doyle, P. S. Rapid microRNA Profiling on Encoded Gel Microparticles. *Angew. Chem., Int. Ed.* **2011**, *50* (10), 2289–2293.
(27) Dempsey, G. T.; Vaughan, J. C.; Chen, K. H.; Bates, M.; Zhuang, X. Evaluation of Fluorophores for Optimal Performance in Localization-Based Super-Resolution Imaging. *Nat. Methods* **2011**, *8* (12), 1027.
(28) Chen, K.; Yan, R.; Xiang, L.; Xu, K. Excitation Spectral Microscopy for Highly Multiplexed Fluorescence Imaging and Quantitative Biosensing. *Light Sci. Appl.* **2021**, *10* (1), 97.
(29) Ali, M. M.; Li, F.; Zhang, Z.; Zhang, K.; Kang, D.-K.; Ankrum, J. A.; Le, X. C.; Zhao, W. Rolling Circle Amplification: A Versatile Tool for Chemical Biology, Materials Science and Medicine. *Chem. Soc. Rev.* **2014**, *43* (10), 3324–3341.
(30) Yao, C.; Zhang, R.; Tang, J.; Yang, D. Rolling Circle Amplification (RCA)-Based DNA Hydrogel. *Nat. Protoc.* **2021**, *16* (12), 5460–5483.
(31) Paul, A.; Farahat, A. A.; Boykin, D. W.; Wilson, W. D. Thermodynamic Factors That Drive Sequence-Specific DNA Binding of Designed, Synthetic Minor Groove Binding Agents. *Life* **2022**, *12* (5), 681.
(32) Deng, R.; Zhang, K.; Wang, L.; Ren, X.; Sun, Y.; Li, J. DNA-Sequence-Encoded Rolling Circle Amplicon for Single-Cell RNA Imaging. *Chem* **2018**, *4* (6), 1373–1386.
(33) Zhao, W.; Ali, M. M.; Brook, M. A.; Li, Y. Rolling Circle Amplification: Applications in Nanotechnology and Biodetection with Functional Nucleic Acids. *Angew. Chem., Int. Ed.* **2008**, *47* (34), 6330–6337.
(34) Loha, K.; Boonkoom, T.; Pitakjakpipop, H.; Alam, I.; Treetong, A.; Boonbanjong, P.; Chatnuntawech, I.; Teerapittayanon, S.; Keyser, U. F.; Schulte, A.; Japrung, D. Structural and Kinetic Profiling of Rolling Circle Amplification via Solid-State Nanopore Sensing Using miR-21 as a Model. *ACS Sens.* **2025**, *10* (9), 7014–7024.
(35) Alfano, C.; Fichou, Y.; Huber, K.; Weiss, M.; Spruijt, E.; Ebbinghaus, S.; De Luca, G.; Morando, M. A.; Vetri, V.; Temussi, P. A.; Pastore, A. Molecular Crowding: The History and Development of a Scientific Paradigm. *Chem. Rev.* **2024**, *124* (6), 3186–3219.
(36) Emmerik, C. L., van; Gachulincova, I.; Lobbia, V. R.; Daniëls, M. A.; Heus, H. A.; Soufi, A.; Nelissen, F. H. T.; Ingen, H., van. Ramified Rolling Circle Amplification for Synthesis of Nucleosomal DNA Sequences. *Anal. Biochem.* **2020**, *588*, 113469.
(37) De la Rosa, C.; Reyes, J. L. Northern Blot Analysis of microRNAs and Other Small RNAs in Plants. *Methods Mol. Biol.* **2019**, *1932*, 121–129.
(38) Xie, F.; Xiao, P.; Chen, D.; Xu, L.; Zhang, B. miRDeepFinder: A miRNA Analysis Tool for Deep Sequencing of Plant Small RNAs. *Plant Mol. Biol.* **2012**, *80* (1), 75–84.
(39) Caruana, J. C.; Dhar, N.; Raina, R. Overexpression of Arabidopsis microRNA167 Induces Salicylic Acid-Dependent Defense against Pseudomonas Syringae through the Regulation of Its Targets ARF6 and ARF8. *Plant Direct* **2020**, *4* (9), e00270.
(40) Merelo, P.; Ram, H.; Pia Caggiano, M.; Ohno, C.; Ott, F.; Straub, D.; Graeff, M.; Cho, S. K.; Yang, S. W.; Wenkel, S.; Heisler, M. G. Regulation of MIR165/166 by Class II and Class III Homeodomain Leucine Zipper Proteins Establishes Leaf Polarity. *Proc. Natl. Acad. Sci. U.S.A.* **2016**, *113* (42), 11973–11978.
(41) Liu, X.; Huang, S.; Xie, H.; Liu, X.; Huang, S.; Xie, H. Advances in the Regulation of Plant Development and Stress Response by miR167. *Front. Biosci. (Landmark Ed)* **2021**, *26* (9), 655–665.
(42) Rodriguez, R. E.; Mecchia, M. A.; Debernardi, J. M.; Schommer, C.; Weigel, D.; Palatnik, J. F. Control of Cell Proliferation in Arabidopsis thaliana by microRNA miR396. *Development* **2010**, *137* (1), 103–112.
(43) Debernardi, J. M.; Rodriguez, R. E.; Mecchia, M. A.; Palatnik, J. F. Functional Specialization of the Plant miR396 Regulatory Network through Distinct MicroRNA–Target Interactions. *PLoS Genet.* **2012**, *8* (1), e1002419.
(44) Hou, N.; Cao, Y.; Li, F.; Yuan, W.; Bian, H.; Wang, J.; Zhu, M.; Han, N. Epigenetic Regulation of miR396 Expression by SWR1-C and the Effect of miR396 on Leaf Growth and Developmental Phase Transition in Arabidopsis. *J. Exp. Bot.* **2019**, *70* (19), 5217–5229.
(45) Li, Y.; Alonso-Peral, M.; Wong, G.; Wang, M.-B.; Millar, A. A. Ubiquitous miR159 Repression of MYB33/65 in Arabidopsis Rosettes Is Robust and Is Not Perturbed by a Wide Range of Stresses. *BMC Plant Biol.* **2016**, *16* (1), 179.
(46) Millar, A. A.; Lohe, A.; Wong, G. Biology and Function of miR159 in Plants. *Plants (Basel)* **2019**, *8* (8), 255.
(47) Yao, X.; Wang, H.; Li, H.; Yuan, Z.; Li, F.; Yang, L.; Huang, H. Two Types of Cis-Acting Elements Control the Abaxial Epidermis-Specific Transcription of the MIR165a and MIR166a Genes. *FEBS Lett.* **2009**, *583* (22), 3711–3717.
(48) Rahimi, A.; Karami, O.; Balazadeh, S.; Offringa, R. miR156-Independent Repression of the Ageing Pathway by Longevity-Promoting AHL Proteins in Arabidopsis. *New Phytol.* **2022**, *235* (6), 2424–2438.
(49) Lawrence, E. H.; Springer, C. J.; Helliker, B. R.; Scott Poethig, R. MicroRNA156-Mediated Changes in Leaf Composition Lead to Altered Photosynthetic Traits during Vegetative Phase Change. *New Phytol.* **2021**, *231* (3), 1008–1022.
(50) Saarenpää, S.; Shalev, O.; Ashkenazy, H.; Carlos, V.; Lundberg, D. S.; Weigel, D.; Giacomello, S. Spatial Metatranscriptomics Resolves Host–Bacteria–Fungi Interactomes. *Nat. Biotechnol.* **2024**, *42* (9), 1384–1393.

Downloaded from http://pubs.acs.org/ascef/article-pdf/doi/10.1021/acssensors.6c01105/6390848/se-2026-01105h.pdf by MASSACHUSETTS INST OF TECHNOLOGY user on 10 August 2026

https://doi.org/10.1021/acssensors.6c01105
ACS Sens. XXXX, XXX, XXX–XXX